Anisotropic magnetoresistance in multiband systems: Two-dimensional electron gases and polar metals at oxide interfaces

Nazim Boudjada, Ilia Khait, and Arun Paramekanti*
Department of Physics, University of Toronto, Toronto, Ontario, Canada M5S1A7

(Received 19 March 2019; revised manuscript received 11 May 2019; published 29 May 2019)

Low-density two-dimensional electron gases (2DEGs) with spin-orbit coupling are highly sensitive to an in-plane magnetic field, which impacts their Fermi surfaces and transport properties. Such 2DEGs, formed at transition metal oxide surfaces or interfaces, can also undergo surface phase transitions leading to polar metals that exhibit electronic nematicity. Motivated by experiments on such systems, we theoretically study magnetotransport in t_{2g} orbital systems, using Hamiltonians that include atomic spin-orbit coupling and broken inversion symmetry, for both square symmetry (001) and hexagonal symmetry (111) 2DEGs. Using a numerical solution to the full multiband matrix-Boltzmann equation, together with insights gleaned from the impurity scattering overlap matrix, we explore the anisotropic magnetoresistance (AMR) in the presence of impurities that favor small momentum scattering. We find that transport in the (001) 2DEG is dominated by a single pair of bands, weakly coupled by impurity scattering, one of which has a larger Fermi velocity while the other provides an efficient current-relaxation mechanism. This leads to strong angle-dependent current damping and a large AMR with many angular harmonics. In contrast, AMR in the (111) 2DEG typically features a single $\cos(2\vartheta)$ harmonic, with the angle-averaged magnetoresistance being highly tunable by a symmetry-allowed trigonal distortion. We also explore how the (111) 2DEG Fermi surfaces are impacted by electronic nematicity via a surface phase transition into a 2D polar metal for which we discuss a Landau theory, and we show that this leads to distinct symmetry components and higher angular harmonics in the AMR. Our results are in qualitative agreement with experiments from various groups for 2DEGs at the $SrTiO_3$ surface and the $LaAlO_3$-$SrTiO_3$ interface.

DOI: 10.1103/PhysRevB.99.195453

I. INTRODUCTION

The ability to control the layer-by-layer growth of transition metal oxide heterostructures has led to the discovery and exploration of two-dimensional electron gases (2DEGs) formed at carefully engineered oxide surfaces and interfaces [1]. Such 2DEGs, formed by a combination of a polarization catastrophe [2] and oxygen vacancies, can combine the multiple functionalities of the two bulk quantum materials forming the interface or potentially host new low-dimensional phases of matter. This has led to a significant focus on magnetism and superconductivity at the (001) $LaAlO_3$-$SrTiO_3$ (LAO-STO) interface [2–26]. Oxide surfaces and interfaces also offer a novel setting to study the role of spin-charge coupling and magnetoelectric effects in 2DEGs [27]. In particular, it has been shown that an electric field can tune the strength of Rashba spin-orbit coupling (SOC), which arises from broken inversion symmetry, permitting control of the Fermi surface (FS) spin-texture and spin-to-charge conversion [8,28,29]. Similarly, an in-plane magnetic field is found to have a significant impact on charge transport, leading to a large negative magnetoresistance in (001) 2DEGs over a range of densities [23,30,31]. More recent experiments have begun to create and probe 2DEGs at oxide (111) surfaces and interfaces [32–41], which have been proposed to host topological phases [42–49]. Such (111) interfaces typically lead to more tightly confined 2DEGs [50].

Transport experiments [22,35–37,39,51] on such 2DEGs have studied the anisotropic magnetoresistance (AMR): the change in the diagonal resistivity when the angle between the current direction and the in-plane magnetic field is varied. AMR has also been studied theoretically in the context of spin-dependent impurity scattering on 2DEG samples with finite magnetization [52,53] and in the context of ferromagnetic semiconductors [54–56]. A useful analysis of the symmetry constraints on the AMR is presented in Ref. [36]. These experiments raise the issues of what controls magnetoresistance in multiband systems such as oxide 2DEGs, why their resistance drops when the magnetic field is rotated from being aligned parallel to the current to being perpendicular to the current direction, and to what extent higher angular harmonics in the AMR directly reflect FS symmetries (e.g., fourfold versus sixfold rotational symmetry of the FS).

Motivated by these questions, we present here a theoretical study of the AMR using a full solution to the semiclassical matrix-Boltzmann equation for the multiband 2DEG with SOC, showing that it captures experimental observations in both (001) and (111) oxide 2DEGs. Focusing on the momentum dependence of the relevant impurity scattering overlap-matrix in the transport equation provides useful insights that are broadly applicable to other multiband systems. Our results also suggest that the AMR harmonics do not directly reflect the underlying lattice rotational symmetries of the FS.

*arunp@physics.utoronto.ca

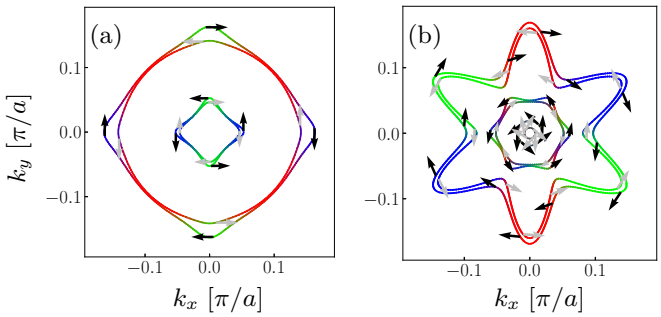

FIG. 1. Fermi surfaces for low-density spin-orbit coupled 2DEGs at zero magnetic field, with colors indicating orbital content (yz-blue, zx-green, xy-red), and Rashba spin texture indicated by black/gray arrows for opposite chiralities. (a) (001) 2DEG at a density $n = 0.035e$/Ti showing outer "circular" bands with significant xy orbital content (except along $k_x = 0$ and $k_y = 0$) and inner "propeller" bands with dominant yz-zx character. (b) (111) 2DEG with $n = 0.05e$/Ti showing outer "flowerlike" bands and inner "hexagon" bands. Each band has equal (momentum-dependent) admixture of all orbitals.

For the (001) 2DEG, our work builds upon previous important numerical studies [23,57]. Here, we further suggest simple physical mechanisms for the observations. At zero magnetic field and low density, Fig. 1(a) shows the FSs and the corresponding Rashba spin texture. We find that an effective Rashba SOC enables weak scattering between a "circular" xy-orbital dominated band and an inner (zx, yz)-orbital dominated "propeller"-band. For small SOC, this interband scattering gets suppressed by an in-plane magnetic field leading to large negative magnetoresistance. Changing the angle of the in-plane magnetic field, we find strong angle-dependent current damping and a large AMR, with many angular harmonics at higher fields, as observed experimentally [30] and in previous theoretical work [23,57].

In striking contrast, transport in the (111) 2DEG is dominated by the outermost pair of "flowerlike" bands, which arise from strong hybridization of *all* three t_{2g} orbitals. The corresponding FSs are shown in Fig. 1(b) along with the Rashba spin texture. While the overall resistivity has some contribution from scattering to an inner small "hexagon" band, the angle dependence of the AMR is dominated by the two large bands. The AMR in this case typically reveals a single $\cos(2\vartheta)$ angular harmonic; although higher harmonics are symmetry-allowed [36], we find they have essentially vanishing weight. Our results are in qualitative agreement with experimental data [36].

Finally, we explore the impact of directional symmetry-breaking on the (111) 2DEG, which leads to a 2D polar metal phase. Such electronic nematicity has been reported in transport experiments [37,51,58]. Polar order in the 2DEG could arise as a result of a bulk structural transition or strong electronic correlations. We argue, within Landau theory, that a polar 2DEG could also arise via a surface phase transition, when the insulating bulk is a paraelectric close to a ferroelectric quantum critical point; this may be of potential relevance to $SrTiO_3$ interfaces. Ferroelectricity in epitaxially strained [111]-oriented $SrTiO_3$ has in fact recently been studied using first-principles calculations [59]. Independent of its microscopic origin, we show that incorporating the nematicity associated with such a polar metal leads to the readily visible violation of some basic symmetry constraints obeyed by the AMR of symmetry-unbroken phases, and also generates higher angular harmonics in the AMR signal. Such simultaneous violations of symmetry constraints and generation of higher harmonics may have been observed in recent experiments at the LAO-STO (111) interface and STO surface.

This paper is organized as follows. We begin with a quick review of the Boltzmann equation for multiband materials, relegating technical details of the computation to Appendix A. We then discuss AMR in the (001) 2DEG and a simplified picture for its origin. We next turn to analogous results for the (111) 2DEG, incorporating the effect of a symmetry-allowed trigonal distortion. Finally, we discuss the impact of directional symmetry breaking on the AMR in (111) 2DEGs in light of recent experimental observations.

II. BOLTZMANN EQUATION

For a weak electric field $\vec{E}$, the semiclassical Boltzmann equation for a multiband system is given by

$$-\frac{\partial f_{n,\mathbf{k}}}{\partial \varepsilon_{n,\mathbf{k}}} eE^i v^i_{n,\mathbf{k}} = \mathcal{N} \sum_m \int \frac{d^2\mathbf{k}'}{(2\pi)^2} (g_{m,\mathbf{k}'} - g_{n,\mathbf{k}}) \times |\langle n\mathbf{k}|\hat{U}|m\mathbf{k}'\rangle|^2 \delta(\varepsilon_{n,\mathbf{k}} - \varepsilon_{m,\mathbf{k}'}), \quad (1)$$

where $f_{n,\mathbf{k}}$ and $g_{n,\mathbf{k}}$ correspond, respectively, to the equilibrium distribution function and its perturbed nonequilibrium part, labeled by band n and momentum $\mathbf{k}$. We use i to denote component indices ($i = x, y$), with implied summation for repeated indices. $\mathcal{N}$ is a constant (proportional to the impurity concentration) that drops out of transport ratio coefficients. The spin-orbit coupled band eigenfunctions, energies, and velocities are denoted by $|n\mathbf{k}\rangle$, $\varepsilon_{n,\mathbf{k}}$, and $v^i_{n,\mathbf{k}}$, respectively; these depend on the magnitude and direction of the applied in-plane magnetic field $\vec{\mathcal{B}}$.

The matrix elements for elastic impurity scattering $\langle n\mathbf{k}|\hat{U}|m\mathbf{k}'\rangle$ are obtained using a scalar scattering potential

$$\hat{U} = \sum_{\mathbf{k},\mathbf{k}',\ell\sigma} V(\mathbf{k} - \mathbf{k}') c^\dagger_{\ell\sigma}(\mathbf{k}') c_{\ell\sigma}(\mathbf{k}), \quad (2)$$

where $V(\mathbf{q}) = V_0 e^{-\Lambda^2|\mathbf{q}|^2/4}$. Setting $\Lambda = 0$ corresponds to scattering off a pointlike impurity, while $\Lambda \gg a$ (with a being the lattice constant) corresponds to small momentum transfer scattering as appropriate for a smooth real-space impurity potential. For $SrTiO_3$, the lattice constant $a \approx 3.9$ Å is the nearest-neighbor Ti-Ti distance in the bulk cubic crystal.

The conductivity tensor within the Boltzmann formalism is then

$$\sigma_{ij} = e^2 \sum_n \int \frac{d^2\mathbf{k}}{(2\pi)^2} v^i_{n,\mathbf{k}} \frac{\partial g_{n,\mathbf{k}}}{\partial E^j}. \quad (3)$$

Here, $\partial g_{n,\mathbf{k}}/\partial E^j$ is computed by taking a derivative of the Boltzmann equation with respect to the electric field, and solving the resulting equations iteratively on a finely discretized momentum mesh in a temperature-dependent window around

the FS. The technical details of this approach, including issues related to choice of the momentum mesh and convergence of the solution, are discussed in Appendix A.

The angle-dependent resistivity tensor is calculated by inverting the conductivity tensor $[\rho(\vartheta)]_{ij} = [\sigma(\vartheta)^{-1}]_{ij}$, where ϑ is the angle between the in-plane magnetic field and the current direction. The AMR and its Fourier amplitudes C_m are defined via

$$\mathrm{AMR}(\vartheta) = \frac{\rho_{xx}(\vartheta) - \rho_{xx}(|\vec{\mathcal{B}}| = 0)}{\rho_{xx}(|\vec{\mathcal{B}}| = 0)}, \tag{4}$$

$$C_m = \int_0^{2\pi} \frac{d\vartheta}{2\pi}\, e^{-im\vartheta}\, \mathrm{AMR}(\vartheta). \tag{5}$$

The invariance of the resistivity under $\vartheta \to \vartheta + \pi$ (which is equivalent to flipping the direction of the current) leads to the vanishing of all odd harmonics C_{2m+1}, while (mirror) symmetry under $\vartheta \to -\vartheta$ yields purely real Fourier coefficients C_m. This latter symmetry is broken for the (111) surface when we include nematic order (see Sec. V).

III. (001) 2DEG

There have been extensive density functional theory studies of the (001) 2DEG [14]. Experiments have realized the (001) 2DEG at the $LaAlO_3$-$SrTiO_3$ interface, and at $SrTiO_3$ surfaces via photodoping [32] or Ar ion bombardment [33,35]. In this last setting, angle-resolved photoemission spectroscopy (ARPES) provides an experimental guide to the FSs of the t_{2g}-orbital derived bands. Based on these, and previous work on magnetotransport [22,23,57], we consider the following model.

A. Model Hamiltonian

We begin with the 2DEG square lattice Hamiltonian in the absence of SOC and a magnetic field:

$$H_0^{001} = \sum_{\mathbf{k}\sigma\ell\ell'} c^\dagger_{\ell\sigma}(\mathbf{k}) \mathcal{M}^{001}_{\ell\ell'}(\mathbf{k}) c_{\ell'\sigma}(\mathbf{k}). \tag{6}$$

Working in the $\{yz, zx, xy\}$ basis, and using abbreviated notation $s_i \equiv \sin(k_i)$, $c_i \equiv \cos(k_i)$ (with $i = x, y$), we have

$$\mathcal{M}^{001} = \begin{pmatrix} \varepsilon_{yz} & \delta_{xy} & i\zeta_x \\ \delta_{xy} & \varepsilon_{zx} & i\zeta_y \\ -i\zeta_x & -i\zeta_y & \varepsilon_{xy} - \Delta_T \end{pmatrix}, \tag{7}$$

where the orbital dispersions are given by

$$\varepsilon_{yz} = 2t_1(1 - c_y) + 2t_2(1 - c_x), \tag{8}$$

$$\varepsilon_{zx} = 2t_1(1 - c_x) + 2t_2(1 - c_y), \tag{9}$$

$$\varepsilon_{xy} = 2t_1(2 - c_x - c_y). \tag{10}$$

Here, t_1 and t_2 are the strong and weak nearest-neighbor intraorbital hoppings, respectively, and $\delta_{xy} \equiv 4t_3 s_x s_y$ is the interorbital next-neighbor hybridization. The tetragonal splitting Δ_T arises from 2D confinement, which lowers the xy-orbital energy, while the odd-in-momentum interorbital hopping $\zeta_i = 2\zeta s_i$ represents the impact of surface inversion breaking.

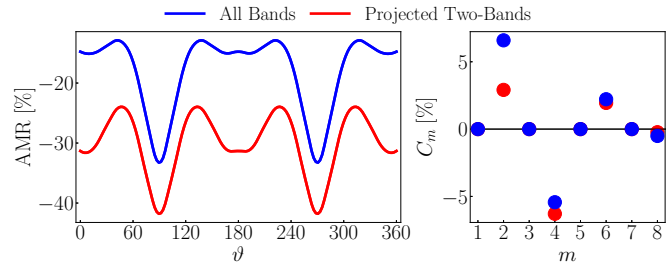

FIG. 2. AMR (left panel) and its Fourier modes (right panel) for the (001) surface computed from the Boltzmann equation. The electronic density is $n = 0.035e$/Ti (which is $2.2 \times 10^{13}/\mathrm{cm}^2$) and the temperature is $T = 10$ K. We fix the magnetic field strength $|\vec{\mathcal{B}}| = 20$ T and vary its angle ϑ with respect to the current, which is along the [100] crystal direction. The impurity scattering length is fixed at $\Lambda = 5a$. The blue curve corresponds to the full solution including all four partially filled bands at the Fermi level, as shown in Fig. 1(a), while the red curve is for the "projected" Boltzmann calculation in which we only retain bands 2 and 3.

Finally, the two important terms for the AMR are the atomic SOC and the coupling to the in-plane magnetic field. SOC is captured by the additional term

$$H_{\mathrm{SOC}} = i\frac{\lambda}{2} \sum_{\mathbf{k}} \epsilon_{\ell mn} c^\dagger_{\ell\sigma}(\mathbf{k}) \tau^n_{\sigma\sigma'} c_{m\sigma'}(\mathbf{k}) \tag{11}$$

(with sums over repeated indices) where $\epsilon_{\ell mn}$ is the Levi-Civita symbol and τ^n are Pauli matrices. Atomic SOC together with the inversion breaking interorbital hopping ζ leads to an effective Rashba SOC. The in-plane magnetic field $\vec{\mathcal{B}}$ leads to the term

$$H_{\mathcal{B}} = (g_\ell \vec{L} + g_s \vec{S}) \cdot \vec{\mathcal{B}}, \tag{12}$$

with orbital and spin g-factors g_ℓ, g_s. Here, the angular momentum components are $L_n = i \sum_{\mathbf{k}} \epsilon_{n\ell m} c^\dagger_{\ell\sigma}(\mathbf{k}) c_{m\sigma}(\mathbf{k})$.

For a quantitative study of the 2DEG, we follow Ref. [23] and fix $(t_1, t_2, t_3, \Delta_T, \zeta, \lambda) \equiv (340, 13, 6, 60, 8, 5)$ meV. We set the orbital g-factor to be $g_\ell = 1$, and the spin g-factor to be $g_s = 5$, with $g_s > 2$ chosen to mimic enhanced ferromagnetic correlations observed in certain such 2DEGs. The transport properties for this system are calculated as a function of the angle ϑ between the in-plane $\vec{\mathcal{B}}$ field and the current (which we assume to run along the [100] crystal axis).

B. Magnetotransport

The zero-field FS for the Hamiltonian $H_0^{001} + H_{\mathrm{SOC}}$ is shown in Fig. 1(a) for $n = 0.035$ electrons per Ti, with colors indicating the orbital content. We also show the corresponding spin texture on each band (with a different color arrow for spin chirality), from which the opposite chirality on pairs of effective Rashba bands is clearly visible. We observe four FSs; the outer two FSs have dominant xy character, with some zx-yz character near the $k_x = 0$ and $k_y = 0$ directions, while the inner two FSs have dominant zx-yz character.

Figure 2(a) shows the calculated AMR signal (blue curve) as a function of magnetic-field angle ϑ, with current along the [100] direction, for $|\vec{B}| = 20$ T, temperature $T = 10$ K, and impurity scattering length $\Lambda = 5a$. We highlight a few

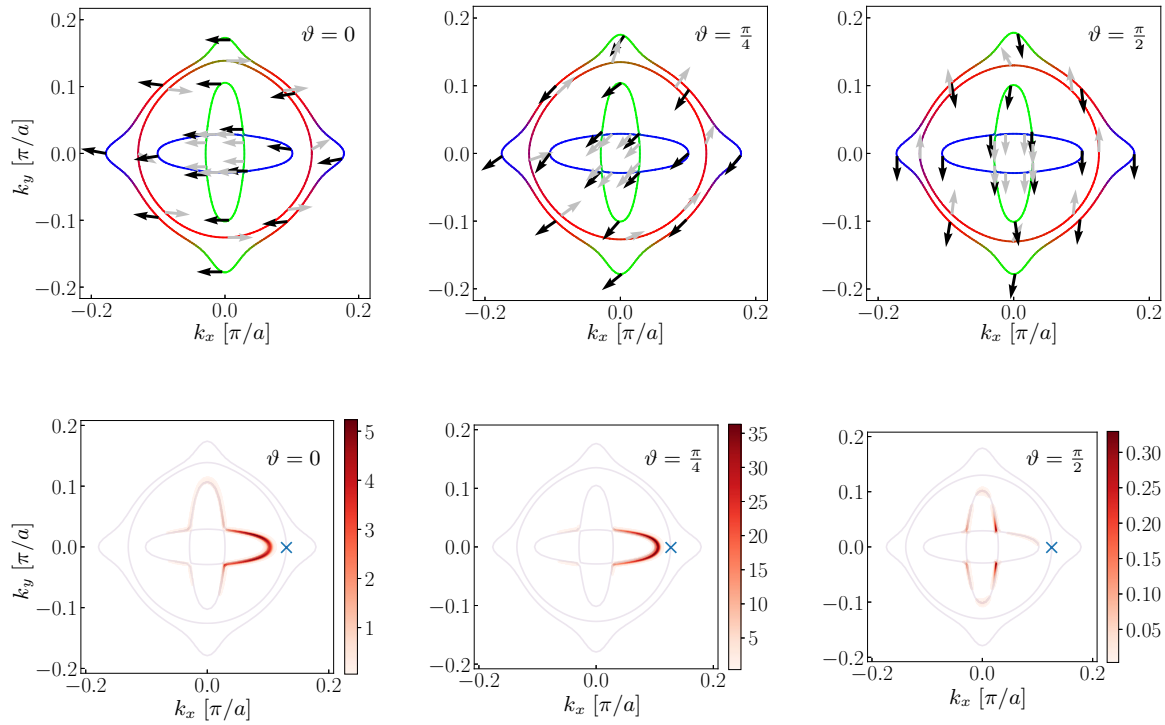

FIG. 3. Top panels: (001) Fermi surfaces and spin textures for fixed magnetic field strength $|\vec{\mathcal{B}}| = 20$ T and various indicated field angles ϑ. Bottom panels: Color-scale plot of impurity scattering overlap matrix, i.e., integrand in the Boltzmann equation, $|\langle n\mathbf{k}|\hat{U}|m\mathbf{k}'\rangle|^2\delta(\varepsilon_{n,\mathbf{k}} - \varepsilon_{m,\mathbf{k}'})$, with $\Lambda = 5a$ for scattering from band $m = 2$ and fixed $\mathbf{k}' = k_F\hat{x}$ (marked by a blue cross) to band $n = 3$ as a function of $\mathbf{k}$ for field angles corresponding to the top panels.

observations from these results: (i) The angle averaged value of the AMR signal indicates a large negative MR as observed in the experiments. (ii) We find that resistivity is significantly lower for fields perpendicular to the current. (iii) From the Fourier modes plotted in Fig. 2(b), we find several nonzero harmonics reflecting the complexity of the AMR signal.

To obtain a simple understanding of these results, we have carried out a detailed analysis to see which bands dominate the AMR. Labeling the four bands as $n = 1, 2, 3, 4$ from the largest to the smallest, we find that the AMR mostly arises from a *single pair* of bands: the "circular" band-2 and the "propeller" band-3. We show the AMR and its harmonic decomposition calculated by projecting to just these two bands in red in Figs. 2(a) and 2(b). In this simplified calculation, we diagonalize the full Hamiltonian for the band wave functions and energies, but retain just the two coupled bands in solving the Boltzmann equation. We see that this two-band system semiquantitatively captures the AMR and its harmonics. To see why this simplified two-band scenario works well, we observe that the outer two bands, derived largely from the xy orbitals, are expected to dominate the diagonal conductivity of the system since they have a larger Fermi surface and a higher Fermi velocity compared with the quasi-1D inner bands. For impurity scattering with small momentum transfer, we also see that intraband scattering will not efficiently degrade the current carried by these bands since it will mostly lead to forward scattering. Thus, the transport lifetime of these bands is limited by interband scattering. Indeed, scattering to the inner "propeller bands" provides an extremely efficient way to degrade current since these bands have a smaller Fermi velocity and a FS shape, which results in their Fermi velocity mostly pointing away from $\hat{x}$.

We emphasize that keeping only two bands has a large impact on the angle-averaged MR (C_0) since the conductivity involves a sum over all bands, and throwing out the largest FS is expected to significantly alter σ_{xx}. However, this procedure correctly captures the angular behavior of the signal. Furthermore, we observe that a more negative AMR is obtained when we restrict the calculation to bands 2 and 3. This is because this procedure involves explicitly switching off the scattering channel between bands 1 and 2, which is expected to lead to very little current decay since the group velocity is very large for both of these bands.

Figures 3(a)–3(c) show the Fermi surface for $\vartheta = 0, \pi/4, \pi/2$. From the spin textures on the FSs, it is clear that the outermost band-1 can continue to scatter strongly to the inner "propeller" band-3 whose shape permits efficient current decay. Thus, band-1 does not have its conduction significantly altered by the magnetic field. However, at this magnetic field, band-2 has its spin nearly antiparallel to the inner band-3 at any field angle while the spins were parallel at zero field [Fig. 1(a)], so any impurity-induced interband scattering to the inner band is strongly suppressed by applying a field. This leads to a magnetic field induced enhancement of transport lifetime for band-2, and a concomitant large negative magnetoresistance.

To further analyze the angle dependence of the AMR, we plot in Figs. 3(a)–3(c) the impurity scattering overlap matrix

$|\langle n\mathbf{k}|\hat{U}|m\mathbf{k}'\rangle|^2\delta(\varepsilon_{n,\mathbf{k}}-\varepsilon_{m,\mathbf{k}'})$, keeping a fixed momentum $\mathbf{k}$ on band-2 indicated by the blue cross (which is the current-carrying region), and for varying momentum $\mathbf{k}'$ on band $m=3$. For $\vartheta=0$ as in Fig. 3(a), we see that the dominant scattering occurs to the forward elongated ellipse part of band-3, which has its Fermi velocity typically directed away from $\hat{x}$, so the resulting transport lifetime will be short. Carriers preferably scatter to this region of the FS because it is closer to the initial momentum, which satisfies the small-momentum transferring potential, and the spins are not fully antiparallel with the spin at $\mathbf{k}$ (marked with the blue $\times$). However, when $\vartheta=\pi/2$ as in Fig. 3(c), the scattering occurs into the vertical ellipse part of band-3, which has its Fermi velocity along $\hat{x}$, leading to less efficient current decay, resulting in a longer transport lifetime. This portion of Fermi momenta is preferred because the previously favored region in the horizontal ellipse now has a fully antiparallel spin with the spin at $\mathbf{k}$. Since the momentum transfer between $\mathbf{k}$ and the vertical ellipse is large, the scattering potential suppresses this scattering channel, which explains the small overlap matrix as seen from the colorbar. Thus, we expect the resistivity to be much lower for $\vartheta=\pi/2$. The reason the spins are not fully parallel or antiparallel stems from the competition between the Rashba energy scale, which becomes important for large Fermi momenta and the magnetic field energy scale. A simple model that captures this behavior is provided in Appendix C. If the ϑ-dependence of this overlap pattern was smooth, we would expect a single $\cos(2\vartheta)$ harmonic in the AMR; however, the pattern at $\vartheta=\pi/4$ [see Fig. 3(b)] is nearly the same as for $\vartheta=0$, so the pattern changes abruptly with angle for $\vartheta>\pi/4$, resulting in many harmonics $\cos(2m\vartheta)$ in the AMR. In particular, the AMR has $\cos(6\vartheta)$ components, which are symmetry-allowed harmonics although the FS itself does not have sixfold symmetry. We do not, at this point, have a simple intuitive understanding of the abrupt change in the overlap matrix for $\vartheta>\pi/4$.

IV. (111) 2DEG

The (111) 2DEG at oxide surfaces and interfaces has also been studied using ARPES [32,34]. Based on such experiments, we can write a general 6×6 Hamiltonian and fit hopping parameters to qualitatively reproduce the shape of the Fermi surfaces seen in experiments.

A. Model Hamiltonian

We begin with the zero-field Hamiltonian

$$H_0^{111}=\sum_{\mathbf{k}\sigma\ell\ell'}c^\dagger_{\ell\sigma}(\mathbf{k})\mathcal{M}^{111}_{\ell\ell'}(\mathbf{k})c_{\ell'\sigma}(\mathbf{k}), \tag{13}$$

defined on a triangular lattice, where

$$\mathcal{M}^{111}=\begin{pmatrix}\varepsilon_{yz} & \gamma_a+i\zeta_{bc}-\frac{\Delta}{3} & \gamma_b-i\zeta_{ac}-\frac{\Delta}{3}\\ \gamma_a-i\zeta_{bc}-\frac{\Delta}{3} & \varepsilon_{zx} & \gamma_c+i\zeta_{ab}-\frac{\Delta}{3}\\ \gamma_b+i\zeta_{ac}-\frac{\Delta}{3} & \gamma_c-i\zeta_{ab}-\frac{\Delta}{3} & \varepsilon_{xy}\end{pmatrix}. \tag{14}$$

Similar to the (001) case, we use the abbreviated notation c_i, s_i, with $\hat{i}=\hat{a},\hat{b},\hat{c}$, where $\hat{a}=\hat{x}$, $\hat{b}=-\hat{x}/2-\hat{y}\sqrt{3}/2$, and $\hat{c}=-\hat{x}/2+\hat{y}\sqrt{3}/2$. With this notation, the intraorbital dispersions are

$$\varepsilon_{yz}=2t_1(1-c_c)+2t_2(2-c_a-c_b), \tag{15}$$

$$\varepsilon_{zx}=2t_1(1-c_b)+2t_2(2-c_c-c_a), \tag{16}$$

$$\varepsilon_{xy}=2t_1(1-c_a)+2t_2(2-c_b-c_c), \tag{17}$$

while the interorbital hybridization $\gamma_i\equiv-2t_3c_i$, the odd-in-momentum term $\zeta_{ij}=2\zeta(s_i+s_j)$ represents hopping permitted by broken inversion symmetry at the interface, and Δ is a symmetry-allowed trigonal distortion term. This Hamiltonian is again supplemented with $H_{\mathrm{SOC}}+H_{\mathcal{B}}$ as for the (001) 2DEG.

The ARPES data on the STO (111) surface [32] are reasonably fit by choosing $(t_1,t_2,t_3)=(320,13,-13)$ meV. In addition, for simplicity, we pick $(\zeta,\lambda)\equiv(8,5)$ meV as for the (001) 2DEG. We also use the same g-factors $g_\ell=1$ and $g_s=5$ for coupling to the in-plane $\vec{\mathcal{B}}$ field, with the field angle ϑ being defined with respect to the $[\bar{1}10]$ crystal axis.

We have explored several values of the symmetry-allowed trigonal distortion scale Δ as shown in Fig. 5. We find that the AMR is reasonably described using values of $\Delta\approx$ 50–80 meV, which are similar to the scale of $\Delta_T=60$ meV in the (001) 2DEG. It is important to note that this local distortion energy scale is different from the band degeneracy splitting at the Γ-point of the BZ; this is given by $6t_3+\Delta$ for the (111) 2DEG, unlike the (001) case, where it is just Δ_T. Furthermore, it has been recently pointed out that this scale can be density-dependent due to renormalization by electron-electron interactions [40,41]. Here, for simplicity, we focus on a single density $n=0.05e$/Ti, and we view Δ as the renormalized distortion.

B. Magnetotransport

For $n=0.05e$/Ti and $\Delta=70$ meV, the (111) 2DEG exhibits four Fermi surfaces with Rashba-like spin textures as shown in Fig. 1(b). The calculated AMR signal for this case is shown as the blue curve in Fig. 4. We find that the magnitude of the angle-averaged MR is smaller than for the (001) case, but it is tunable by changing the trigonal distortion Δ as seen from Fig. 5. In all cases, we find that the AMR has C_2 character, with no sign of higher harmonics. This is qualitatively consistent with experimental observations. We have found that this C_2 dominant response, with almost no sign of higher harmonics, holds true even up to much higher densities $n\sim0.4e$/Ti.

To understand the average MR, we plot the spin texture on the FSs in Fig. 6 at nonzero $\vec{\mathcal{B}}$, which shows that there is a significant contrast with the (001) 2DEG—namely, the outer pair of bands features opposite spin polarizations, and so does the inner pair of bands. As a result, each outer band (band-1 or band-2) has a corresponding inner band (band-3 or band-4) into which it can scatter even when $\mathcal{B}\neq0$; this leads to a reduced MR, since no scattering channel is "switched off" by the field unlike in the (001) 2DEG. The tunability of the MR with Δ arises due to changes in the FS spin textures, such

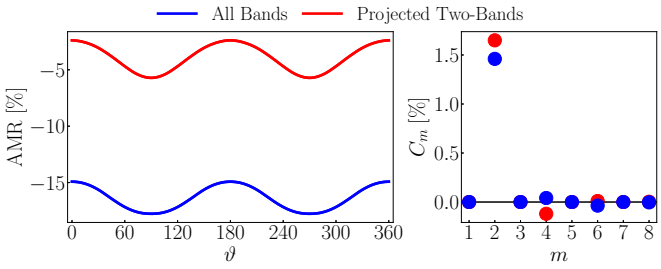

FIG. 4. AMR (left) and its Fourier modes (right) for the (111) surface for electronic density $n = 0.05e$/Ti (corresponding to 1.6×10^{13} cm^2) and at $T = 5$ K. The strength of the magnetic field is kept constant at $|\vec{\mathcal{B}}| = 20$ T and its angle ϑ is varied with respect to the current, which is along the $[\bar{1}10]$ crystal direction. The impurity scattering length is taken to be $\Lambda = 5a$. Similar to Fig. 2, the blue curve is the solution obtained when keeping all Fermi surfaces shown in Fig. 1(b), while the red curve is obtained when only keeping the two outermost "flowerlike" bands 1 and 2.

that an inner band flips its spin polarization; the mechanism for large negative MR then parallels that of the (001) 2DEG.

We observe that the projected two-band calculation leads to a more positive angle-averaged AMR, unlike in the (001) case. This is specific to the choice of Δ presented here, and is not a universal feature. Indeed, since the (111) surface is mainly governed by the outermost FSs, which have large velocities, no efficient current-degrading scattering channel is switched-off when the calculation is projected to these two outer bands. For this reason, whether the projected or the full calculation leads to the most negative C_0 coefficient is more difficult to predict and depends on the choice of parameters.

The sign of the C_2 harmonic in the AMR may be understood from the overlap matrix plots in Fig. 6. It is clear that both $\vartheta = 0$ and $\vartheta = \pi/2$ have scattering from the marked blue cross on band-1 to momenta on band-2 where the Fermi velocity points away from $\hat{x}$, leading to current dissipation. However, for $\vartheta = \pi/2$, the magnitude of this overlap is smaller (see the color scale), and furthermore it has some scattering into band-2 where the Fermi velocity is still along $\hat{x}$, which suppresses the resistivity for this field angle.

We attribute the absence of higher harmonics in the AMR signal to the fact that each band in the (111) 2DEG has an equal (momentum-dependent) mixture of all three orbitals

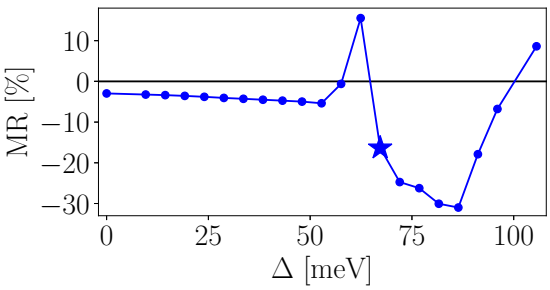

FIG. 5. Effect of trigonal distortion Δ on the (111) MR at a fixed density $n = 0.05e$/Ti and a temperature $T = 5$ K. The point marked $\star$ corresponds to $\Delta = 70$ meV, which is used to compute the full AMR signal.

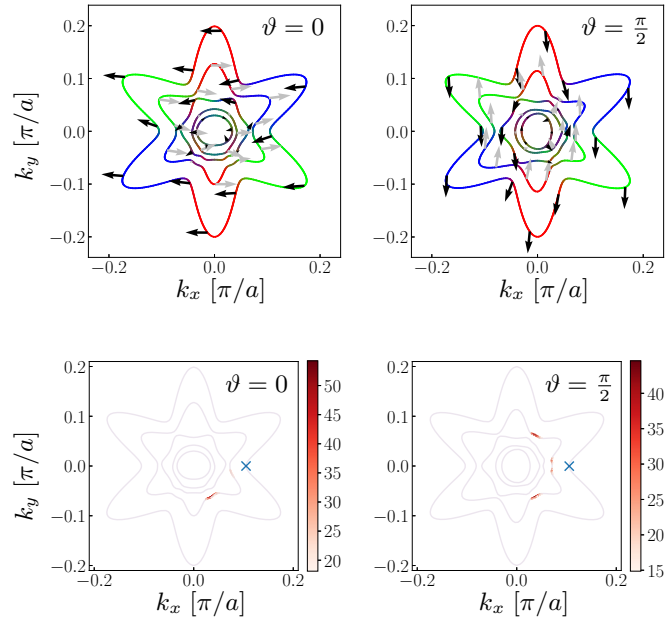

FIG. 6. Top panel: (111) Fermi surfaces and spin textures at nonzero magnetic field $|\vec{\mathcal{B}}| = 20$ T for $\vartheta = 0, \pi/2$; black/gray arrows indicate spin textures on bands with opposite Rashba spin chiralities at zero field. Bottom panel: Integrand of the Boltzmann equation $|\langle n\mathbf{k}|\hat{U}|m\mathbf{k}'\rangle|^2 \delta(\varepsilon_{n,\mathbf{k}} - \varepsilon_{m,\mathbf{k}'})$ with $\Lambda = 5a$ for scattering from fixed band $m = 1$ and $\mathbf{k}' = k_F\hat{x}$ (marked with a blue $\times$) to band $n = 2$ as a function of final momentum $\mathbf{k}$.

yz, zx, xy, which independently have strong directional character. This is different from the (001) 2DEG where the more unidirectional yz, zx orbitals are split off from the symmetric xy orbitals.

V. IMPACT OF SYMMETRY BREAKING IN THE (111) 2DEG: A 2D POLAR METAL

We turn next to the question of how directional symmetry breaking at the (111) interface, which leads to a 2D polar metal phase, might impact the AMR in the 2DEG. Our work is partly motivated by experimental reports of nematicity in transport measurements in such 2DEGs [35–37,41,58]. Such symmetry breaking might have its origin in the bulk 3D structure; e.g., bulk $SrTiO_3$ has a structural cubic-to-tetragonal transition upon lowering temperature [60] $T \lesssim 100$ K. If the tetragonal domains are aligned, it will impose a nematic distortion for 2DEGs at the surface or interface of such a crystal. In high-density 2DEGs, symmetry breaking may also be driven by electron interactions [61], which can lead to orbital-ordering or cause a Pomeranchuk instability of the FS. Finally, as discussed in the Introduction, the surface or interface hosting the 2DEG might undergo a surface phase transition, leading to a polar metal breaking discrete rotational and mirror symmetries of the 2DEG.

A. Landau theory and coupling to electrons

Independent of its microscopic origin, the order parameter for such a nematic in (111) 2DEGs is a complex scalar ψ, with

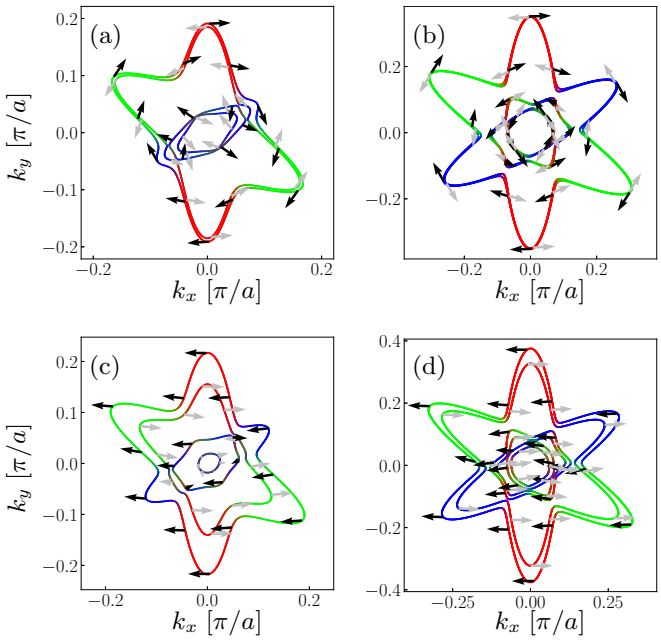

FIG. 7. FSs and spin textures in the nematic 2DEG (polar metal), with couplings $v_1 = v_2 = -11$ meV and phase $\chi = \pi$ in Eq. (20), at two different densities: (a) $n = 0.05e$/Ti and (b) $0.2e$/Ti. The impact of $\psi \neq 0$ is more visually pronounced at smaller densities. Panels (c) and (d) show corresponding FSs at nonzero field $|\vec{\mathcal{B}}| = 20$ T. In panels (a) and (b), arrows of different colors (black/gray) belong to FSs that are almost degenerate (and hence difficult to resolve visually) but which come with opposite chiralities.

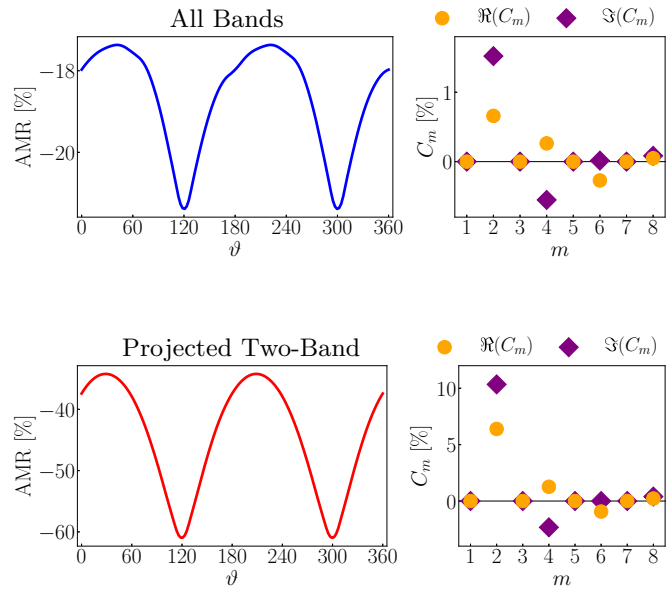

FIG. 8. AMR (left) and its Fourier modes (right) for the (111) surface for electronic density $n = 0.05e$/Ti including the symmetry-breaking order parameter ψ with $v_1 = v_2 = -11$ meV and $\chi = \pi$. The top panels show the AMR signal including all bands while the bottom panels are results from the projected calculation using band-1 and band-4. In the Fourier-mode panels, circles and diamonds represent the real and imaginary parts of the different Fourier components C_m; the imaginary part is permitted in this case due to the symmetry-breaking field ψ, which results in breaking $\vartheta \to -\vartheta$ symmetry of the AMR. Note that the maxima of the AMR signal are shifted away from $\vartheta = 0, \pi$.

the Landau theory taking the form

$$\mathcal{F}_{111} = r|\psi|^2 + w(\psi^3 + \psi^{*3}) + u|\psi|^4 + \cdots, \qquad (18)$$

where cubic terms lead to an effective Z_3 clock model. A similar model was studied long ago for bulk $SrTiO_3$ in the presence of a stress applied along the (111) direction [62]. We present a heuristic derivation of this in Appendix B, discussing its relation to the proximity of $SrTiO_3$ to a paraelectric-ferroelectric quantum phase transition.

The impact of this symmetry breaking is captured by a local linear-in-ψ coupling to the orbitals via

$$\begin{aligned} H_\psi = &-\tfrac{1}{2}\tilde{v}_1\left[\left(L_x^2+\omega L_y^2+\omega^2 L_z^2\right)\psi + \text{H.c.}\right] \\ &-\tfrac{1}{2}\tilde{v}_2[(\overline{L_yL_z}+\omega\overline{L_zL_x}+\omega^2\overline{L_xL_y})\,\psi + \text{H.c.}], \end{aligned} \qquad (19)$$

where $\omega = e^{i2\pi/3}$, and we have defined the symmetrized product $\overline{L_iL_j} = L_iL_j + L_jL_i$. Explicitly, this leads to an orbital Hamiltonian

$$H_\psi = \begin{pmatrix} v_1\cos(\chi) & v_2\cos\left(\chi+\frac{4\pi}{3}\right) & v_2\cos\left(\chi+\frac{2\pi}{3}\right) \\ v_2\cos\left(\chi+\frac{4\pi}{3}\right) & v_1\cos\left(\chi+\frac{2\pi}{3}\right) & v_2\cos(\chi) \\ v_2\cos\left(\chi+\frac{2\pi}{3}\right) & v_2\cos(\chi) & v_1\cos\left(\chi+\frac{4\pi}{3}\right) \end{pmatrix}, \qquad (20)$$

where we have set $\psi = |\psi|e^{i\chi}$, and absorbed the amplitude of the order parameter into redefined coefficients $v_{1,2} = |\psi|\tilde{v}_{1,2}$, which have dimensions of energy.

The resulting distorted FSs and their spin textures are shown in Fig. 7 at two different densities $n = 0.05e$/Ti and $n = 0.2e$/Ti. For illustrative purposes, we have chosen $v_1 = v_2 = -11$ meV and $\chi = \pi$. We find that the observed distortion of the FS is harder to resolve at higher densities where ARPES studies [32,34] have been carried out on the (111) surface 2DEG of $SrTiO_3$.

B. Magnetotransport

The AMR in the presence of this symmetry breaking field, with $v_1 = v_2 = -11$ meV and $\chi = \pi$, is shown in Fig. 8. We find that the AMR exhibits several new aspects absent in the symmetric 2DEG: (i) The AMR is no longer symmetric under $\vartheta \to -\vartheta$, which allows for sinusoidal components in the Fourier decomposition. (ii) We find higher angular harmonics being generated by the symmetry breaking. These observations appear consistent with experiments [36], where the onset of higher C_6 harmonics in the AMR appears to coincide with the breaking of the $\vartheta \to -\vartheta$ symmetry of the signal, suggesting that these two phenomena go hand in hand, and might be tied to directional symmetry breaking in the 2DEG. As shown in Fig. 8, all of these results, including the correct sign of the Fourier modes, can be qualitatively reproduced by keeping just a single pair of bands in solving the Boltzmann equation. Unlike the non-symmetry-broken phase discussed previously, the relevant bands are now bands 1 and 4 which have different shapes and orbital content—the outermost band is mainly composed of xy, zx orbitals while the innermost band has a predominant yz character. This situation is similar

to the (001) calculation where the relevant bands 2 and 3 had different geometries/orbital contents leading us to believe that this orbital imbalance and different geometry could be responsible for the generation of higher harmonics.

VI. SUMMARY AND DISCUSSION

We have considered model 2D Hamiltonians for both (001) and (111) oxide interface 2DEGs, and we showed that their AMR is in reasonable agreement with experimental results. Such simplified model Hamiltonians are thus useful to describe the transport properties of these 2DEGs. Our results, obtained by solving the full matrix Boltzmann equation, may be rationalized in terms of simplified two-band models and from the momentum dependence of the scattering overlap matrix. We summarize below some of the key results and discuss some speculative ideas:

(i) We have shown that the MR and its angle dependence in the oxide 2DEGs appear to be governed by the field-dependent tuning of interband scattering.

(ii) Octahedral distortions, such as the trigonal distortion at the (111) interface, can significantly affect the FSs and MR, suggesting that engineering or tuning such distortions may provide a viable route to controlling transport properties of such 2DEGs.

(iii) We have argued, and provided a Landau theory reasoning, for why (111) oxide interfaces might stabilize polar metal phases, particularly those involving $SrTiO_3$, which are proximate to a bulk ferroelectric critical point. Our work suggests that the AMR and its symmetries may be used to indirectly detect such symmetry breaking. Furthermore, the nematic resistivity observed [37,51,58] in insulating ultralow density (111) 2DEGs may be viewed as arising from an "Anderson-localized polar metal," which exhibits anisotropic variable-range hopping. It would be interesting to further explore this regime.

(iv) While the dominant AMR mode is the uniform C_2 angular component, we have shown that higher harmonics can emerge in symmetric (001) 2DEGs and in nematic/polar (111) 2DEGs. In particular, the higher AMR harmonics appear not to be directly related to FS symmetries. However, a common emerging picture, based on comparing the (001) and (111) 2DEGs, is that these harmonics may arise from a shape mismatch between the two bands that govern the AMR.

(v) Various experiments on the metallic (111) 2DEGs report a change in the AMR when cooling below $T^* \lesssim$ 20–25 K, which depends on density and is consistent with underlying polar symmetry breaking. This may reflect the actual symmetry-breaking temperature scale of the 2DEG, or it might reflect a temperature at which the 2DEG effectively "approaches" the symmetry-broken interface, with the polar order onset already occurring at a higher transition temperature. Future studies of this issue would be valuable.

(vi) The concavity or convexity of the 2DEG FS is known to strongly impact Hall transport in perpendicular magnetic fields [53,56]. Here, we have focused on the diagonal resistivity under an in-plane magnetic field, and it is unclear how much the AMR is impacted under these circumstances by the FS curvature. We find that multiband scattering plays a more important role.

(vii) Finally, we have considered the simple case of scattering off a scalar impurity (independent of orbital and spin) in this paper. A future direction would be to study orbital-dependent impurity scattering and the impact of spin-orbit randomness [63,64] using the scattering overlap matrix to provide insights.

ACKNOWLEDGMENTS

We thank Venkat Chandrasekhar, Yoram Dagan, and Bill Atkinson for useful discussions about oxide 2DEGs, and Ehud Altman for insightful conversations about the possible connection between nematic/polar order of the 2DEG and the proximity of $SrTiO_3$ to a ferroelectric phase. This work was supported by Discovery Grant from NSERC of Canada, the CIfAR Quantum Materials Programme, and FRQNT of Quebec. This research was enabled in part by support provided by Compute Ontario, Westgrid, and Compute Canada. Computations were performed on the Niagara supercomputer at the SciNet HPC Consortium. SciNet is funded by the Canada Foundation for Innovation, the Government of Ontario, Ontario Research Fund–Research Excellence, and the University of Toronto.

APPENDIX A: NUMERICAL SOLUTION OF THE BOLTZMANN EQUATION

It is helpful to rewrite Eq. (1) with discretized momenta as

$$-\frac{\partial f_{n,\mathbf{k}}}{\partial \varepsilon_{n,\mathbf{k}}} E^i v^i_{n,\mathbf{k}} = \sum_{m,l,\mathbf{k}',\mathbf{k}''} (\delta_{nl}\delta_{\mathbf{k},\mathbf{k}''} - \delta_{ml}\delta_{\mathbf{k}',\mathbf{k}''}) g_{l,\mathbf{k}''} \times |\langle n\mathbf{k}|\hat{U}|m\mathbf{k}'\rangle|^2 \, \delta(\varepsilon_{n,\mathbf{k}} - \varepsilon_{m,\mathbf{k}'}), \quad \text{(A1)}$$

where we have dropped the factors of $(\mathcal{N}, e)$ since we will only be interested in *ratios* of transport coefficients where these will cancel. Taking a derivative with respect to E^i, and lumping together band and momentum indices via $\mu \equiv (n, \mathbf{k})$, $\nu \equiv (m, \mathbf{k}')$, and $\alpha \equiv (l, \mathbf{k}'')$, we get

$$\left(-\frac{\partial f}{\partial \varepsilon} v^i\right)_\mu = \sum_{\nu,\alpha} (\delta_{\alpha\mu} - \delta_{\alpha\nu}) |U_{\mu\nu}|^2 \delta(\varepsilon_\mu - \varepsilon_\nu) \left(\frac{\partial g}{\partial E^i}\right)_\alpha \equiv \sum_\alpha (A_{\mu\alpha} - B_{\mu\alpha}) \left(\frac{\partial g}{\partial E^i}\right)_\alpha, \quad \text{(A2)}$$

where $U_{\mu\nu} \equiv \langle\mu|\hat{U}|\nu\rangle$, $B_{\mu\alpha} \equiv |\langle\mu|\hat{U}|\alpha\rangle|^2 \delta(\varepsilon_\mu - \varepsilon_\alpha)$, and $A_{\mu\alpha} \equiv \sum_\nu B_{\mu\nu}\delta_{\mu\alpha}$. Equation (A2) is a matrix inversion problem for the "vector" $(\partial g/\partial E^i)$; however, $(A - B)^{-1}$ is not well defined since it has a zero eigenvalue associated with a constant (band and momentum-independent) vector $(\partial g/\partial E^i) \propto \mathbb{1}$.

Rather than using SVD algorithms and pseudoinverse techniques, we found that an efficient way to solve Eq. (A2) is to write it as an iterative equation

$$\left[\frac{\partial g}{\partial E^i}\right]_{p+1} = A^{-1}\left(B\left[\frac{\partial g}{\partial E^i}\right]_p - \frac{\partial f}{\partial \varepsilon} v^i\right). \quad \text{(A3)}$$

We begin at step $p = 0$ by guessing a random initial vector $[\partial g/\partial E^i]_{p=0}$, removing its projection in the constant eigenvector subspace, and evaluating the right-hand side of the above

equation to obtain a new $[\partial g/\partial E^i]_{p=1}$. We then repeat this process, taking care at each step to remove the projection of $[\partial g/\partial E^i]_p$ to the constant eigenvector (to avoid errors that can creep in from numerical precision). Convergence is reached when the L_2 norm $||\frac{\partial f}{\partial \varepsilon} v^i + (A - B)\frac{\partial g}{\partial E^i}||_2 <$ tol, where tol is typically chosen to be 10^{-10}.

We find that for proper convergence one must choose momentum mesh sizes of the order 2500×2500 for temperatures of $T \sim 5$ K. Since the (A, B) matrix dimensions scale as $(6 \times 2500^2 \times 6 \times 2500^2)$ for a six-band problem, the memory requirements far exceed what can be handled by clusters. To reduce the dimensionality of the problem, we use the fact that g and $\partial g/\partial E^i$ must go to zero far from the Fermi momenta and work with momenta within a certain temperature T window of the Fermi momenta. It is found that a temperature window of $\pm 6 \times T$ is reasonable for low densities ($n \lesssim 0.1$) while one needs up to $\pm 12 \times T$ at high densities $n \gtrsim 0.4$.

APPENDIX B: LANDAU THEORY OF NEMATIC/POLAR 2DEG

We start with the Landau theory for ferroelectric order in a bulk 3D cubic crystal in terms of the vector order parameter $\vec{\varphi} = (\varphi_x, \varphi_y, \varphi_z)$ representing the electric dipole moment vector. In a displacive ferroelectric, this arises due to displacements of the ions away from high symmetry positions; for instance, in $BaTiO_3$ or ^{18}O isotope-substituted $SrTiO_3$, it would involve off-center displacements of the Ba^{2+} or Sr^{2+} ions from the cube center, and the Ti^{4+} ions within the oxygen octahedra. The (x, y, z) components refer to the cubic axes of crystal. The symmetry-allowed bulk terms are

$$\mathcal{F}_{\text{bulk}} = r_B\vec{\varphi}^2 + u_B\vec{\varphi}^4 + w_B\left(\varphi_x^4 + \varphi_y^4 + \varphi_z^4\right), \tag{B1}$$

with subscript B on the coefficients denoting bulk. Explicit spatiotemporal gradients of the order parameter, stemming from thermal or quantum fluctuation effects, are ignored here; they are only taken into account to the extent that they renormalize the coefficients of this effective Landau theory. Here, $r_B \propto (T - T_c)$, where T_c is the mean-field ordering temperature in the 3D ferroelectric state. Since $SrTiO_3$ remains a paraelectric, it has $r_B > 0$ down to the lowest temperature, but proximity to a quantum critical point can lead to small $r_B(T = 0)$. Even in such cases, where the bulk remains paraelectric, a spontaneous symmetry-breaking state might still arise at the surface.

With $\hat{n} \parallel [111]$, additional terms are allowed at the surface,

$$\begin{aligned}\Delta\mathcal{F}_{111} = {} & \alpha\vec{\varphi}\cdot\hat{n} + g(\vec{\varphi}\cdot\hat{n})^2 + \lambda_1(\vec{\varphi}\cdot\hat{n})^3 + \lambda_2(\vec{\varphi}\cdot\hat{n})\vec{\varphi}^2 \\ & + \lambda_3\varphi_x\varphi_y\varphi_z + w_1(\vec{\varphi}\cdot\hat{n})^4 + w_2(\vec{\varphi}\cdot\hat{n})^2\vec{\varphi}^2 \\ & + w_3\left(\varphi_x^2\varphi_y^2 + \varphi_y^2\varphi_z^2 + \varphi_z^2\varphi_x^2\right).\end{aligned} \tag{B2}$$

From the bulk free energy, $w_B < 0$ favors states in which the dipole moment points along [100] or symmetry-related axes for a total of six symmetry-related ground states. At a (111) surface, the inversion-breaking term α splits this sixfold degeneracy into two triplets $(+\hat{x}, +\hat{y}, +\hat{z})$ and $(-\hat{x}, -\hat{y}, -\hat{z})$. Any symmetry-breaking surface phase transitions will involve breaking the residual C_3 and mirror symmetries of these triplets.

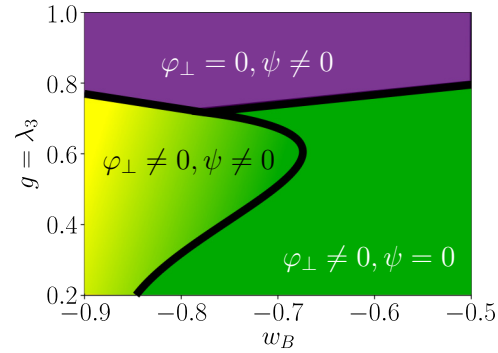

FIG. 9. Phase diagram of the Landau theory, given by Eqs. (B1) and (B2), as a function of w_B and $g = \lambda_3$, keeping all other coefficients fixed as indicated in the text, and where $\varphi_\perp$ and ψ are defined in Eq. (B3). The phase with $\psi = 0$ is a "paraelectric" phase, and it is associated with a moment pointing along $\hat{n}$ (which is always symmetry allowed at a surface or interface), while the phases with $\psi \neq 0$ are symmetry-broken phases, having purely in-plane ($\varphi_\perp = 0$) or partially in-plane ($\varphi_\perp \neq 0$) electric dipole moments. Conduction electrons will convert these symmetry-broken phases with $\psi \neq 0$ into 2D polar metals.

Similarly, $w_B > 0$ in the bulk free energy favors the eight degenerate states where the dipole moment points along [111] and its symmetry equivalents. At the (111) surface, $g > 0$ breaks this degeneracy into a high-energy doublet (with dipoles along $\pm\hat{n}$) and a low-energy sextet with dipoles along the other directions: $(11\bar{1})$, $(1\bar{1}1)$, $(\bar{1}11)$, $(1\bar{1}\bar{1})$, $(\bar{1}1\bar{1})$, and $(\bar{1}\bar{1}1)$. The term α splits this low-energy sextet into two triplets $[(11\bar{1}), (1\bar{1}1), (\bar{1}11)]$ and $[(1\bar{1}\bar{1}), (\bar{1}1\bar{1}), (\bar{1}\bar{1}1)]$. As for the case with $w_B < 0$, the residual surface symmetry breaking will involve breaking C_3 and mirror symmetries.

As an illustrative example, we plot the phase diagram of such a Landau theory in Fig. 9. Here, we choose to work in units where the bulk Landau theory coefficient $u_B = 1$, we set $r_B = 0.01$, and we vary w_B. For the surface coefficients, we set $\alpha = -0.2$, $\lambda_1 = \lambda_2 = 0$, and we drop quartic invariants $w_1 = w_2 = w_3 = 0$ while varying $g = \lambda_3$. Since the surface breaks $\hat{n} \to -\hat{n}$ inversion, it is useful to parametrize

$$\vec{\varphi} \equiv \varphi_\perp\hat{n} + \psi\vec{\gamma} + \psi^*\vec{\gamma}^*, \tag{B3}$$

where $\hat{n} \equiv (1, 1, 1)/\sqrt{3}$, $\vec{\gamma} \equiv (1, \omega, \omega^2)/\sqrt{3}$, and $\omega = e^{i2\pi/3}$. Here, $\varphi_\perp$ is a non-symmetry-breaking polarization, while the complex $\psi \neq 0$ reflects spontaneous symmetry breaking of the surface symmetries.

We can simplify the Landau theory to focus only on the in-plane spontaneous symmetry-breaking order parameter ψ. Substituting the above expression in the free energy $\mathcal{F} + \Delta\mathcal{F}_{111}$, we arrive at the simplified free energy at the (111) surface,

$$\mathcal{F}_{111} = r|\psi|^2 + w(\psi^3 + \psi^{*3}) + u|\psi|^4 + \cdots, \tag{B4}$$

used in the main text. In the absence of conduction electrons, the state with $\psi \neq 0$ is a nematic that breaks rotational symmetry. Due to the symmetry-allowed cubic term w which breaks $\psi \to -\psi$ symmetry, it is also a surface ferroelectric with an in-plane ferroelectric moment. The conducting 2DEG

at the surface will convert this into a "polar metal" phase, which exhibits nematic transport.

APPENDIX C: TWO-BAND MODEL

To get some insight about the sign of the C_2 Fourier coefficient, we consider the following Hamiltonian in the $\{|\uparrow\rangle, |\downarrow\rangle\}$ basis, with a continuum Rashba term and a Zeeman field:

$$H(\mathbf{k}) = \varepsilon^0_{\mathbf{k}}\sigma_0 + \lambda(\vec{\sigma} \times \mathbf{k}) \cdot \hat{z} + \tilde{g}\vec{\mathcal{B}} \cdot \vec{\sigma}. \tag{C1}$$

The eigenvalues and eigenvectors are given by

$$\varepsilon_{\mathbf{k},\pm} = \varepsilon^0_{\mathbf{k}} \pm \sqrt{\lambda^2|\mathbf{k}|^2 + g^2|\vec{\mathcal{B}}|^2 + 2\lambda\tilde{g}(k_y\mathcal{B}_x - k_x\mathcal{B}_y)}, \tag{C2}$$

$$|u_\pm(\mathbf{k})\rangle = \frac{1}{\sqrt{2}}(\pm e^{i\phi_{\mathbf{k}}}, 1)^T, \tag{C3}$$

where $\tan(\phi_{\mathbf{k}}) \equiv (\frac{\lambda k_x - g\mathcal{B}_y}{\lambda k_y + \tilde{g}\mathcal{B}_x})$. At a given electronic density, one can calculate the overlaps between points $\mathbf{k}$ and $\mathbf{k} + \delta\mathbf{k}$ both sitting at the Fermi level of two bands with different chirality. For a scalar scattering potential, we can only focus on the eigenstates overlaps:

$$|\langle u_\pm(\mathbf{k} + \delta\mathbf{k})|u_\mp(\mathbf{k})\rangle|^2 = \sin^2\left(\frac{\phi_{\mathbf{k}+\delta\mathbf{k}} - \phi_{\mathbf{k}}}{2}\right), \tag{C4}$$

$$|\langle u_\pm(\mathbf{k} + \delta\mathbf{k})|u_\pm(\mathbf{k})\rangle|^2 = \cos^2\left(\frac{\phi_{\mathbf{k}+\delta\mathbf{k}} - \phi_{\mathbf{k}}}{2}\right). \tag{C5}$$

Parametrizing the in-plane components in polar coordinates via $\vec{\mathcal{B}} = |\vec{\mathcal{B}}|(\cos\vartheta, \sin\vartheta)$, $\mathbf{k} = |\mathbf{k}|(\cos\alpha, \sin\alpha)$, $\delta\mathbf{k} = |\delta\mathbf{k}|(\cos\beta, \sin\beta)$, and rescaling $g = \tilde{g}|\vec{\mathcal{B}}|$, we can expand to leading order in λ/g (large magnetic field limit) and g/λ (large Rashba limit):

$$|\langle u_\pm(\mathbf{k} + \delta\mathbf{k})|u_\mp(\mathbf{k})\rangle|^2 \overset{\frac{\lambda}{g}\to 0}{=} \frac{|\delta\mathbf{k}|^2\lambda^2}{4g^2}\cos^2(\beta - \vartheta) + O\left[\left(\frac{\lambda}{g}\right)^3\right], \tag{C6}$$

$$|\langle u_\pm(\mathbf{k} + \delta\mathbf{k})|u_\mp(\mathbf{k})\rangle|^2 \overset{\frac{g}{\lambda}\to 0}{=} \sin^2\left(\frac{\alpha - \beta}{2}\right) + O\left(\frac{g}{\lambda}\right). \tag{C7}$$

From this, it is clear that in the large field limit the overlap is minimal for $\beta = \vartheta \pm \frac{\pi}{2}$ and its maximum is when $\beta = \{\vartheta, \vartheta \pm \pi\}$, independently of the position of $\mathbf{k}$. In other words, the spins on each band will either align or antialign with the magnetic field. In the large Rashba limit we distinguish two cases: (i) for $|\delta\mathbf{k}| > |\mathbf{k}|$ the overlap is maximized when $\beta = \alpha \pm \pi$, and (ii) for $|\delta\mathbf{k}| < |\mathbf{k}|$ it is maximized for $\beta = \alpha \pm \cos^{-1}(-|\delta\mathbf{k}|/|\mathbf{k}|)$. The details of this will be determined by the explicit shape of the scattering potential and the scattering length scale. For a point at $k_y = 0$, i.e., $\alpha = 0$ like those considered in Figs. 3 and 6, the two overlaps (C6) and (C7) can be simultaneously maximized for a field in the x-direction by choosing $\beta = \pm\pi$ leading to an overall higher resistivity. On the other hand, for a field pointing in the y direction no choice of β can maximize the two overlaps, giving rise to a competition between the Rashba and magnetic field energy scales and thus reducing the total overlap and resistivity.

[1] J. Chakhalian, J. W. Freeland, A. J. Millis, C. Panagopoulos, and J. M. Rondinelli, *Colloquium*: Emergent properties in plane view: Strong correlations at oxide interfaces, Rev. Mod. Phys. **86**, 1189 (2014).

[2] N. Nakagawa, H. Y. Hwang, and D. A. Muller, Why some interfaces cannot be sharp, Nat. Mater. **5**, 204 (2006).

[3] A. Ohtomo and H. Y. Hwang, A high-mobility electron gas at the $LaAlO_3/SrTiO_3$ heterointerface, Nature (London) **427**, 423 (2004).

[4] S. Thiel, G. Hammerl, A. Schmehl, C. W. Schneider, and J. Mannhart, Tunable quasi-two-dimensional electron gases in oxide heterostructures, Science **313**, 1942 (2006).

[5] M. Takizawa, H. Wadati, K. Tanaka, M. Hashimoto, T. Yoshida, A. Fujimori, A. Chikamatsu, H. Kumigashira, M. Oshima, K. Shibuya, T. Mihara, T. Ohnishi, M. Lippmaa, M. Kawasaki, H. Koinuma, S. Okamoto, and A. J. Millis, Photoemission from Buried Interfaces in $LaAlO_3/SrTiO_3$ Superlattices, Phys. Rev. Lett. **97**, 057601 (2006).

[6] N. Reyren, S. Thiel, A. D. Caviglia, L. F. Kourkoutis, G. Hammerl, C. Richter, C. W. Schneider, T. Kopp, A.-S. Rüetschi, D. Jaccard, M. Gabay, D. A. Muller, J.-M. Triscone, and J. Mannhart, Superconducting interfaces between insulating oxides, Science **317**, 1196 (2007).

[7] A. D. Caviglia, S. Gariglio, N. Reyren, D. Jaccard, T. Schneider, M. Gabay, S. Thiel, G. Hammerl, J. Mannhart, and J.-M. Triscone, Electric field control of the $LaAlO_3/SrTiO_3$ interface ground state, Nature (London) **456**, 624 (2008).

[8] A. D. Caviglia, M. Gabay, S. Gariglio, N. Reyren, C. Cancellieri, and J.-M. Triscone, Tunable Rashba Spin-Orbit Interaction at Oxide Interfaces, Phys. Rev. Lett. **104**, 126803 (2010).

[9] T. Ariando, X. Wang, G. Baskaran, Z. Q. Liu, J. Huijben, J. B. Yi, A. Annadi, A. Roy Barman, A. Rusydi, S. Dhar, Y. P. Feng, J. Ding, H. Hilgenkamp, and T. Venkatesan, Electronic phase separation at the $LaAlO_3/SrTiO_3$ interface, Nat. Commun. **2**, 188 (2011).

[10] J. A. Bert, B. Kalisky, C. Bell, M. Kim, Y. Hikita, H. Y. Hwang, and K. A. Moler, Direct imaging of the coexistence of ferromagnetism and superconductivity at the $LaAlO_3/SrTiO_3$ interface, Nat. Phys. **7**, 767 (2011).

[11] L. Li, C. Richter, J. Mannhart, and R. C. Ashoori, Coexistence of magnetic order and two-dimensional superconductivity at $LaAlO_3/SrTiO_3$ interfaces, Nat. Phys. **7**, 762 (2011).

[12] G. Khalsa and A. H. MacDonald, Theory of the $SrTiO_3$ surface state two-dimensional electron gas, Phys. Rev. B **86**, 125121 (2012).

[13] M. M. Mehta, D. A. Dikin, C. W. Bark, S. Ryu, C. M. Folkman, C. B. Eom, and V. Chandrasekhar, Evidence for charge-vortex duality at the $LaAlO_3/SrTiO_3$ interface, Nat. Commun. **3**, 955 (2012).

[14] Z. Zhong, A. Tóth, and K. Held, Theory of spin-orbit coupling at $LaAlO_3/SrTiO_3$ interfaces and $SrTiO_3$ surfaces, Phys. Rev. B **87**, 161102(R) (2013).

[15] K. Michaeli, A. C. Potter, and P. A. Lee, Superconducting and Ferromagnetic Phases in $SrTiO_3/LaAlO_3$ Oxide Interface Structures: Possibility of Finite Momentum Pairing, Phys. Rev. Lett. **108**, 117003 (2012).

[16] L. Fidkowski, H.-C. Jiang, R. M. Lutchyn, and C. Nayak, Magnetic and superconducting ordering in one-dimensional nanostructures at the $LaAlO_3/SrTiO_3$ interface, Phys. Rev. B **87**, 014436 (2013).

[17] M. H. Fischer, S. Raghu, and E.-A. Kim, Spin-orbit coupling in $LaAlO_3/SrTiO_3$ interfaces: magnetism and orbital ordering, New J. Phys. **15**, 023022 (2013).

[18] Y. Kim, R. M. Lutchyn, and C. Nayak, Origin and transport signatures of spin-orbit interactions in one- and two-dimensional $SrTiO_3$-based heterostructures, Phys. Rev. B **87**, 245121 (2013).

[19] S. Banerjee, O. Erten, and M. Randeria, Ferromagnetic exchange, spin-orbit coupling and spiral magnetism at the $LaAlO_3/SrTiO_3$ interface, Nat. Phys. **9**, 626 (2013).

[20] G. Chen and L. Balents, Ferromagnetism in Itinerant Two-Dimensional t_{2g} Systems, Phys. Rev. Lett. **110**, 206401 (2013).

[21] S. Y. Park and A. J. Millis, Charge density distribution and optical response of the $LaAlO_3/SrTiO_3$ interface, Phys. Rev. B **87**, 205145 (2013).

[22] J. Ruhman, A. Joshua, S. Ilani, and E. Altman, Competition between Kondo screening and magnetism at the $LaAlO_3/SrTiO_3$ interface, Phys. Rev. B **90**, 125123 (2014).

[23] M. Diez, A. M. R. V. L. Monteiro, G. Mattoni, E. Cobanera, T. Hyart, E. Mulazimoglu, N. Bovenzi, C. W. J. Beenakker, and A. D. Caviglia, Giant Negative Magnetoresistance Driven by Spin-Orbit Coupling at the $LaAlO_3/SrTiO_3$ Interface, Phys. Rev. Lett. **115**, 016803 (2015).

[24] S. Nandy, N. Mohanta, S. Acharya, and A. Taraphder, Anomalous transport near the Lifshitz transition at the $LaAlO_3/SrTiO_3$ interface, Phys. Rev. B **94**, 155103 (2016).

[25] J. R. Tolsma, M. Polini, and A. H. MacDonald, Orbital and spin order in oxide two-dimensional electron gases, Phys. Rev. B **95**, 205101 (2017).

[26] W. A. Atkinson, P. Lafleur, and A. Raslan, Influence of the ferroelectric quantum critical point on $SrTiO_3$ interfaces, Phys. Rev. B **95**, 054107 (2017).

[27] A. A. Burkov, A. S. Núñez, and A. H. MacDonald, Theory of spin-charge-coupled transport in a two-dimensional electron gas with Rashba spin-orbit interactions, Phys. Rev. B **70**, 155308 (2004).

[28] E. Lesne, Y. Fu, S. Oyarzun, J. C. Rojas-Sánchez, D. C. Vaz, H. Naganuma, G. Sicoli, J. P. Attané, M. Jamet, E. Jacquet, J. M. George, A. Barthélémy, H. Jaffrès, A. Fert, M. Bibes, and L. Vila, Highly efficient and tunable spin-to-charge conversion through Rashba coupling at oxide interfaces, Nat. Mater. **15**, 1261 (2016).

[29] Q. Song, H. Zhang, T. Su, W. Yuan, Y. Chen, W. Xing, J. Shi, J. Sun, and W. Han, Observation of inverse Edelstein effect in Rashba-split 2DEG between $SrTiO_3$ and $LaAlO_3$ at room temperature, Sci. Adv. **3**, e1601614 (2017).

[30] M. Ben Shalom, C. W. Tai, Y. Lereah, M. Sachs, E. Levy, D. Rakhmilevitch, A. Palevski, and Y. Dagan, Anisotropic magnetotransport at the $SrTiO_3/LaAlO_3$ interface, Phys. Rev. B **80**, 140403(R) (2009).

[31] X. Wang, W. M. Lü, A. Annadi, Z. Q. Liu, K. Gopinadhan, S. Dhar, T. Venkatesan, and Ariando, Magnetoresistance of two-dimensional and three-dimensional electron gas in $LaAlO_3/SrTiO_3$ heterostructures: Influence of magnetic ordering, interface scattering, and dimensionality, Phys. Rev. B **84**, 075312 (2011).

[32] T. C. Rödel, C. Bareille, F. Fortuna, C. Baumier, F. Bertran, P. Le Fèvre, M. Gabay, O. Hijano Cubelos, M. J. Rozenberg, T. Maroutian, P. Lecoeur, and A. F. Santander-Syro, Orientational Tuning of the Fermi Sea of Confined Electrons at the $SrTiO_3$ (110) and (111) Surfaces, Phys. Rev. Appl. **1**, 051002 (2014).

[33] S. McKeown Walker, A. de la Torre, F. Y. Bruno, A. Tamai, T. K. Kim, M. Hoesch, M. Shi, M. S. Bahramy, P. D. C. King, and F. Baumberger, Control of a Two-Dimensional Electron Gas on $SrTiO_3$(111) by Atomic Oxygen, Phys. Rev. Lett. **113**, 177601 (2014).

[34] L. Dudy, M. Sing, P. Scheiderer, J. D. Denlinger, P. Schäetz, J. Gabel, M. Buchwald, C. Schlueter, T.-L. Lee, and R. Claessen, *In situ* control of separate electronic phases on $SrTiO_3$ surfaces by oxygen dosing, Adv. Mater. **28**, 7443 (2016).

[35] L. Miao, R. Du, Y. Yin, and Q. Li, Anisotropic magnetotransport properties of electron gases at $SrTiO_3$ (111) and (110) surfaces, Appl. Phys. Lett. **109**, 261604 (2016).

[36] P. K. Rout, I. Agireen, E. Maniv, M. Goldstein, and Y. Dagan, Six-fold crystalline anisotropic magnetoresistance in (111) $LaAlO_3/SrTiO_3$ oxide interface, Phys. Rev. B **95**, 241107(R) (2017).

[37] S. K. Davis, Z. Huang, K. Han, T. Ariando, T. Venkatesan, and V. Chandrasekhar, Electrical transport anisotropy controlled by oxygen vacancy concentration in (111) $LaAlO_3/SrTiO_3$ interface structures, Adv. Mater. Interf. **4**, 1600830 (2017).

[38] A. M. R. V. L. Monteiro, D. J. Groenendijk, I. Groen, J. de Bruijckere, R. Gaudenzi, H. S. J. van der Zant, and A. D. Caviglia, Two-dimensional superconductivity at the (111) $LaAlO_3/SrTiO_3$ interface, Phys. Rev. B **96**, 020504(R) (2017).

[39] S. Davis, Z. Huang, K. Han, Ariando, T. Venkatesan, and V. Chandrasekhar, Anisotropic superconductivity and frozen electronic states at the (111) $LaAlO_3/SrTiO_3$ interface, Phys. Rev. B **98**, 024504 (2018).

[40] A. M. R. V. L. Monteiro, M. Vivek, D. J. Groenendijk, P. Bruneel, I. Leermakers, U. Zeitler, M. Gabay, and A. D. Caviglia, Band inversion driven by electronic correlations at the (111) $LaAlO_3/SrTiO_3$ interface, Phys. Rev. B **99**, 201102 (2019).

[41] U. Khanna, P. K. Rout, M. Mograbi, G. Tuvia, I. Leermakers, U. Zeitler, Y. Dagan, and M. Goldstein, Symmetry and correlation effects on band structure explain the anomalous transport properties of (111) $LaAlO_3/SrTiO_3$, arXiv:1901.10931 (cond-mat.str-el).

[42] D. Xiao, W. Zhu, Y. Ran, N. Nagaosa, and S. Okamoto, Interface engineering of quantum Hall effects in digital transition metal oxide heterostructures, Nat. Commun. **2**, 596 (2011).

[43] A. Rüegg and G. A. Fiete, Topological insulators from complex orbital order in transition-metal oxides heterostructures, Phys. Rev. B **84**, 201103(R) (2011).

[44] A. M. Cook and A. Paramekanti, Double Perovskite Heterostructures: Magnetism, Chern Bands, and Chern Insulators, Phys. Rev. Lett. **113**, 077203 (2014).

[45] S. Okamoto, W. Zhu, Y. Nomura, R. Arita, D. Xiao, and N. Nagaosa, Correlation effects in (111) bilayers of perovskite transition-metal oxides, Phys. Rev. B **89**, 195121 (2014).

[46] X. Hu, Z. Zhong, and G. A. Fiete, First principles prediction of topological phases in thin films of pyrochlore iridates, Sci. Rep. **5**, 11072 (2015).

[47] S. Baidya, U. V. Waghmare, A. Paramekanti, and T. Saha-Dasgupta, High-temperature large-gap quantum anomalous Hall insulating state in ultrathin double perovskite films, Phys. Rev. B **94**, 155405 (2016).

[48] L. Si, O. Janson, G. Li, Z. Zhong, Z. Liao, G. Koster, and K. Held, Quantum Anomalous Hall State in Ferromagnetic $SrRuO_3$ (111) Bilayers, Phys. Rev. Lett. **119**, 026402 (2017).

[49] H.-S. Kim and H.-Y. Kee, Realizing Haldane model in Fe-based honeycomb ferromagnetic insulators, npj Quantum Mater. **2**, 20 (2017).

[50] S. Baidya, U. V. Waghmare, A. Paramekanti, and T. Saha-Dasgupta, Controlled confinement of half-metallic two-dimensional electron gas in $BaTiO_3/Ba_2FeReO_6/BaTiO_3$ heterostructures: A first-principles study, Phys. Rev. B **92**, 161106(R) (2015).

[51] S. Davis, V. Chandrasekhar, Z. Huang, K. Han, Ariando, and T. Venkatesan, Anisotropic multicarrier transport at the (111) $LaAlO_3/SrTiO_3$ interface, Phys. Rev. B **95**, 035127 (2017).

[52] R. Burgos, J. H. Warnes, and N. De La Espriella, Anisotropic magnetoresistance in 2DEG with Rashba spin-orbit coupling, J. Magn. Magn. Mater. **466**, 234 (2018).

[53] M. Trushin, K. Výborný, P. Moraczewski, A. A. Kovalev, J. Schliemann, and T. Jungwirth, Anisotropic magnetoresistance of spin-orbit coupled carriers scattered from polarized magnetic impurities, Phys. Rev. B **80**, 134405 (2009).

[54] T. McGuire and R. L. Potter, Anisotropic magnetoresistance in ferromagnetic 3D alloys, IEEE Trans. Magn. **11**, 1018 (1975).

[55] K. Y. Wang, K. W. Edmonds, R. P. Campion, L. X. Zhao, C. T. Foxon, and B. L. Gallagher, Anisotropic magnetoresistance and magnetic anisotropy in high-quality (Ga,Mn)As films, Phys. Rev. B **72**, 085201 (2005).

[56] E. De Ranieri, A. W. Rushforth, K. Výborný, U. Rana, E. Ahmad, R. P. Campion, C. T. Foxon, B. L. Gallagher, A. C. Irvine, J. Wunderlich, and T. Jungwirth, Lithographically and electrically controlled strain effects on anisotropic magnetoresistance in (Ga,Mn)As, New J. Phys. **10**, 065003 (2008).

[57] N. Bovenzi and M. Diez, Semiclassical theory of anisotropic transport at $LaAlO_3/SrTiO_3$ interfaces under an in-plane magnetic field, Phys. Rev. B **95**, 205430 (2017).

[58] S. Davis, Z. Huang, K. Han, Ariando, T. Venkatesan, and V. Chandrasekhar, Signatures of electronic nematicity in (111) $LaAlO_3/SrTiO_3$ interfaces, Phys. Rev. B **97**, 041408(R) (2018).

[59] S. E. Reyes-Lillo, K. M. Rabe, and J. B. Neaton, Ferroelectricity in [111]-oriented epitaxially strained $SrTiO_3$ from first principles, Phys. Rev. Mater. **3**, 030601 (2019).

[60] A. Aharony, K. A. Müller, and W. Berlinger, Trigonal-to-Tetragonal Transition in Stressed $SrTiO_3$: A Realization of the Three-State Potts Model, Phys. Rev. Lett. **38**, 33 (1977).

[61] N. Boudjada, G. Wachtel, and A. Paramekanti, Magnetic and Nematic Orders of the Two-Dimensional Electron Gas at Oxide (111) Surfaces and Interfaces, Phys. Rev. Lett. **120**, 086802 (2018).

[62] K. Alex Müller, W. Berlinger, and E. Tosatti, Indication for a novel phase in the quantum paraelectric regime of $SrTiO_3$, Z. Phys. B **84**, 277 (1991).

[63] V. K. Dugaev, M. Inglot, E. Ya. Sherman, J. Berakdar, and J. Barnaś, Nonlinear Anomalous Hall Effect and Negative Magnetoresistance in a System with Random Rashba Field, Phys. Rev. Lett. **109**, 206601 (2012).

[64] N. Bovenzi, S. Caprara, M. Grilli, R. Raimondi, N. Scopigno, and G. Seibold, Density inhomogeneities and rashba spin-orbit coupling interplay in oxide interfaces, J. Phys. Chem. Solids (2017), doi:10.1016/j.jpcs.2017.09.013.